Magnetic and electrical properties of (Pu,Lu)Pd_3

M. D. Le

*Helmholtz-Zentrum Berlin für Materialen und Energie, Hahn-Meitner-Platz 1, D-14109 Berlin, Germany**

K. A. McEwen

Department of Physics and Astronomy, and London Centre for Nanotechnology, University College London, WC1E 6BT, UK

E. Colineau, J.-C. Griveau, and R. Eloirdi

European Commission, Joint Research Centre, Institute for Transuranium Elements, Postfach 2340, 76125 Karlsruhe, Germany

(Dated: September 13, 2010)

We present measurements of the magnetic susceptibility, heat capacity and electrical resistivity of $Pu_{1-x}Lu_xPd_3$, with x=0, 0.1, 0.2, 0.5, 0.8 and 1. $PuPd_3$ is an antiferromagnetic heavy fermion compound with $T_N = 24$ K. With increasing Lu doping, both the Kondo and RKKY interaction strengths fall, as judged by the Sommerfeld coefficient γ and Néel temperature T_N. Fits to a crystal field model of the resistivity also support these conclusions. The paramagnetic effective moment $\mu_{\rm eff}$ increases with Lu dilution, indicating a decrease in the Kondo screening. In the highly dilute limit, $\mu_{\rm eff}$ approaches the value predicted by intermediate coupling calculations. In conjunction with an observed Schottky peak at $\sim$60 K in the magnetic heat capacity, corresponding to a crystal field splitting of $\sim$12 meV, a mean-field intermediate coupling model with nearest neighbour interactions has been developed.

I. INTRODUCTION

The $AnPd_3$ series of compounds, with An=U, Np, or Pu, are rare examples of actinide intermetallic compounds in which the $5f$ electrons are well localised around the ionic sites. UPd_3 is a very interesting compound which exhibits four quadrupolar ordered phases below 8K[1], whilst there are indications that $NpPd_3$ may also show quadrupolar order at low temperatures[2]. These two compounds crystallise in the double-hexagonal close-packed (dhcp) structure, in contrast to $PuPd_3$ which adopts the $AuCu_3$ structure, with lattice parameter a =4.105Å. This reflects the increasing localisation of the $5f$ electrons as shown by recent photoelectron spectroscopy measurements[3].

Early measurements of the bulk properties and neutron diffraction studies[4] show it to be antiferromagnetic, with a transition temperature $\sim$24 K, and a G-type structure, where nearest neighbour moments are aligned antiparallel. The same study found that the high temperature resistivity shows a Kondo-like behaviour, increasing with decreasing temperature. This behaviour, together with a high Sommerfeld coefficient deduced from recent heat capacity measurements[5], led us to make a further investigation of the properties of $PuPd_3$.

Our aim has been to study how the competition between the Kondo effect and the RKKY exchange interaction affects the physical properties of this compound. This may be accomplished by doping with a non-magnetic ion, which increases the distance between localised f-electrons, and hence decreases the RKKY interaction. Finally, the single-ion properties of the Pu ion may be investigated in the highly di-

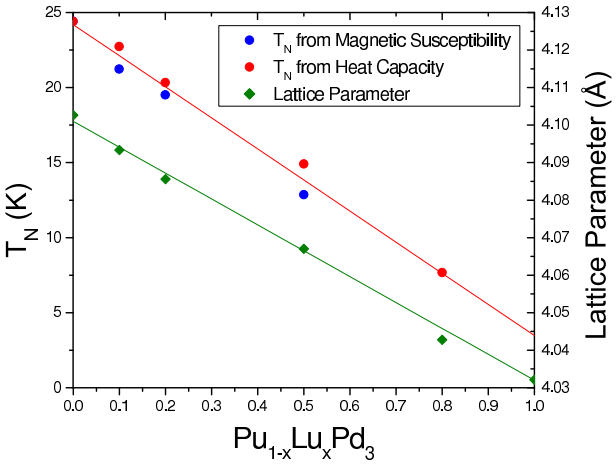

FIG. 1: (Color online) Lattice parameters and transition temperatures for $Pu_{1-x}Lu_xPd_3$.

lute limit.

In this work, we present in section II the experimental details and in section III the measurements of the magnetic susceptibility, and heat capacity of $Pu_{1-x}Lu_xPd_3$. These measurements are then analysed using a localised moment mean field model in section IV. Finally, section V presents measurements of the electrical resistivity and Hall coefficient of $Pu_{1-x}Lu_xPd_3$, which are assessed in terms of a simple crystal field model.

II. EXPERIMENTAL DETAILS

Polycrystalline samples of $PuPd_3$, $LuPd_3$ and $Pu_{1-x}Lu_xPd_3$, with $x = 0.1$, 0.2, 0.5, and 0.8, were produced at ITU by arc melting appropriate amounts of the constituent elements under a high purity argon atmosphere on a water-cooled copper hearth, using a Zr getter. The $AuCu_3$ structure was confirmed by x-ray diffraction for each sample, and the lattice parameters are shown in figure 1. The data show a linear dependence of the lattice parameter with increasing Lu dilution, in accordance with Vegard's Law, which also confirms the stoichiometry of the samples. In addition, there also appears to be a linear dependence of the transition temperature, T_N, with doping. These temperatures were determined from magnetic susceptibility, χ, and heat capacity, C_p, measurements described in the next section. At T_N there is a maximum in χ, and hence this temperature was determined by numerically differentiating the data to find $\frac{d\chi}{dT} = 0$. In the heat capacity there is a lambda step at T_N, which was determined by differentiating the data to find the minima of $\frac{dC_p}{dT}$. The values of T_N deduced from these two measurements are in close agreement, whereas the inflexion points of the resistivity data do not correlate with T_N as determined from χ or C_p. Nevertheless, the resistivity inflexion points show the same decreasing trend with Lu-doping as T_N. Errors in T_N quoted in table I were determined by the width in temperature of the lambda step for C_p or the step in $\frac{d\chi}{dT}$.

The magnetisation and susceptibility were measured using a SQUID magnetometer (Quantum Design MPMS-7), whilst the heat capacity was determined by the hybrid adiabatic relaxation method in a Quantum Design PPMS-9 for $PuPd_3$ and $LuPd_3$, and in a PPMS-14 for $Pu_{1-x}Lu_xPd_3$. Small samples were used for the heat capacity measurements (from 1.5 mg for $PuPd_3$ to ≈5 mg for other compositions) so that the decay heat does not significantly affect the measurements. The X-ray diffraction, magnetisation and heat capacity measurements were made immediately after the preparation of samples in order to minimise the effects of radiation damage.

Finally, thin parallel-sided samples of each composition were extracted, polished and mounted for electrical transport measurements. As these measurements were made some three months after synthesis, we observed significant radiation damage which manifested in a high residual resistivity at low temperatures. This prompted us to re-anneal the samples at 800° C for 12 h, and to remeasure the electrical transport properties. The remeasured data is presented in section V.

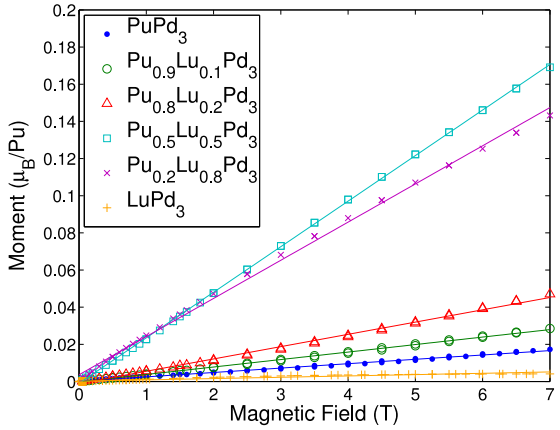

FIG. 2: (Color online) The magnetisation at 10 K of $Pu_{1-x}Lu_xPd_3$.

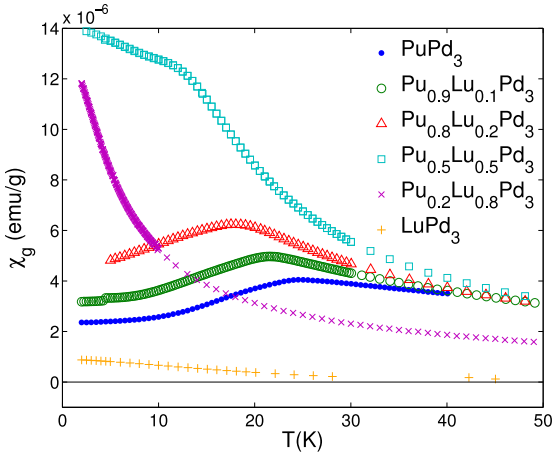

FIG. 3: (Color online) The magnetic susceptibility of $Pu_{1-x}Lu_xPd_3$.

III. MAGNETISATION AND HEAT CAPACITY MEASUREMENTS

A. Magnetisation

Figure 2 shows the magnetisation at 10 K, which is generally linear with field, and is not saturated at 7 T. This is not surprising because we expect a $J = 5/2$ ion to be saturated at a field $\gtrsim 100$ T, when the splitting between the lowest two CF levels is $\gg$10 K. The magnetic susceptibility is shown in figure 3, and the inverse susceptibility in figure 4. The data in the paramagnetic phase above the Néel temperature are well fitted by a modified Curie-Weiss Law

$$\frac{M}{H} = \frac{N\mu_{\rm eff}^2\mu_B^2}{3k_B}\frac{1}{T-\theta_{\rm CW}} + \chi_0(H) \qquad (1)$$

where N is the number of Pu atoms in the compound, and $\theta_{\rm CW}$ is the paramagnetic Curie temperature. We recall that in the Weiss mean field theory, ($-\theta_{\rm CW}$) $\theta_{\rm CW}$ corresponds to the (anti-) ferromagnetic transition temperature. However, this theory does not take into account single ion effects such as the crystal field which are expected to be significant in $PuPd_3$.

There is a field dependent residual susceptibility $\chi_0(H)$ which mainly arises from impurities, the encapsulation and the sample holder. In addition, the Pauli susceptibility of the conduction electrons may also contribute to χ_0 and can be estimated from the electronic Sommerfeld coefficient of $LuPd_3$, $\gamma^+_{LuPd_3}$=3.2(1) mJmol^{-1}K^{-2}, which yields $\chi_{\rm Pauli} \approx 5.2(2) \times 10^{-5}\mu_B$/T-f.u. This is significantly lower than the observed values of

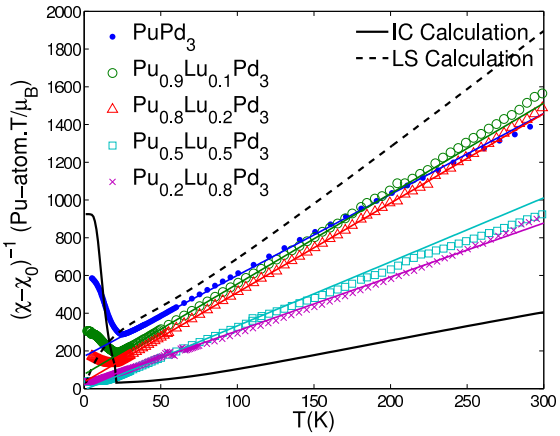

FIG. 4: (Color online) The inverse magnetic susceptibility of $Pu_{1-x}Lu_xPd_3$. Thin solid lines are fits to the modified Curie-Weiss Law for each compound. The mean field intermediate coupling calculation is shown as a thick solid line, whilst the dashed line shows the single ion susceptibility calculated from the crystal field in *LS*-coupling.

the residual susceptibility, which are of the order of 10^{-3} μ_B/T-f.u., indicating that the conduction electron susceptibility contribution is negligible. The fitted parameters to the Curie-Weiss relation for each sample are given in table I. The quoted error is deduced from ... Figure 4 shows the inverse susceptibility of the different compositions with the residual susceptibility χ_0 subtracted.

The magnitudes of the effective moments are all significantly higher than the *LS*-coupling value, 0.85 μ_B. Any crystal field interaction will only decrease this effective moment because as the crystal field split levels become further separated and hence thermally de-occupied, their angular momentum will cease to contribute to the moment. The effective moment with zero crystal field splitting in *intermediate coupling* on the other hand is approximately 1.4 μ_B, as calculated using the theory outlined in section IV. This value may be decreased slightly by a large crystal field, and suggests that we should use intermediate coupling to calculate the single-ion properties of Pu^{3+}.

An alternative reason for the higher than expected effective moment may be due to some high moment paramagnetic impurity. However, analysis of the x-ray diffraction patterns showed that the only impurity is Lu_2O_3 which is non-magnetic. There may also be some trace amounts of oxides of Pu which is not observed in the diffraction pattern. PuO_2 is a Van Vleck paramagnet[6] which may contribute to the impurity term in equation 1, whilst Pu_2O_3 is an antiferromagnet with an effective moment of 2.1 μ_B[7]. However, one would need approximately 6 mol % Pu_2O_3 in $PuPd_3$ order for it be responsible for the increased effective moment compared to the *LS*-coupling expectation, at which concentration it should be detectable in the X-ray diffraction pattern, which is not the case. Furthermore, the enhanced value of μ_{eff} for Pu_2O_3 which also has a free ion Pu^{3+} configuration suggests that intermediate coupling is appropriate in these cases.

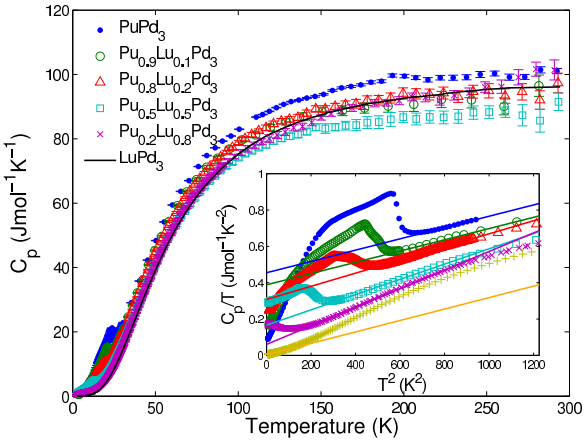

FIG. 5: (Color online) Heat capacity of $Pu_{1-x}Lu_xPd_3$ at zero applied magnetic field. The inset shows C_p/T vs T^2 and solid lines there show fits to $C/T \sim \gamma + AT^2$. $LuPd_3$ data is shown in orange in the inset

B. Heat Capacity

The heat capacity at zero field is shown in figure 5, whilst details of the results in applied fields up to 14 T are in figure 6. We note that at high temperatures, C_p tends to the classical Dulong-Petit limit, $3NR = 99.8$ Jmol^{-1}K^{-1}. For $Pu_{0.9}Lu_{0.1}Pd_3$, the derivative in the heat capacity shows two minima, which stem from the step-like nature of the transition. The higher temperature inflexion point at $\sim$22 K corresponds well with the peak in the inverse susceptibility, but the lower temperature peak at $\sim$21 K does not match any feature in the magnetic susceptibility. Nevertheless, these two anomalies raise the possibility that there may indeed be two transitions in this compound. Moreover, as can be seen in Figure 6, the heat capacity of $Pu_{0.8}Lu_{0.2}Pd_3$ also shows indications of two transitions.

An estimate of the electronic specific heat $C_{\rm el} = \gamma T$ and Debye temperature θ_D was obtained using the approximation

$$C \sim \gamma T + \frac{12\pi^4 N_A k_B}{5}\left(\frac{T^3}{\theta_D^3}\right) \qquad (2)$$

which is valid at low temperatures ($T \ll \theta_D$),

Composition	T_N (K)		$\gamma^{\pm}$(mJ/mol.K^2)		θ_D (K)	$\mu_{\rm eff}$ (μ_B/Pu)	$\theta_{\rm CW}$ (K)
	C_p	χ	$T > T_N$	$T < 8$ K	$T > T_N$		
$PuPd_3$	24.4(3)	24.9(4)		75(1)	306(19)	1.02(1)	-39.9(1)
$Pu_{0.9}Lu_{0.1}Pd_3$	22.7(4)	22.5(1)		133(8)	304(18)	0.97(2)	-15.8(2)
$Pu_{0.8}Lu_{0.2}Pd_3$	20(1)	19.5(1)		221(14)	280(6)	0.97(2)	-7.5(2)
$Pu_{0.5}Lu_{0.5}Pd_3$	15(1)	12.8(1)	183(36)	289(10)	270(10)	1.15(2)	1.8(1)
$Pu_{0.2}Lu_{0.8}Pd_3$	7(2)		99(49)	170(5)	257(13)	1.25(1)	-7.2(2)
$LuPd_3$				3.5(5)	291(12)		

TABLE I: Transition temperatures and other parameters derived from the magnetic susceptibility and heat capacity of $Pu_{1-x}Lu_xPd_3$.

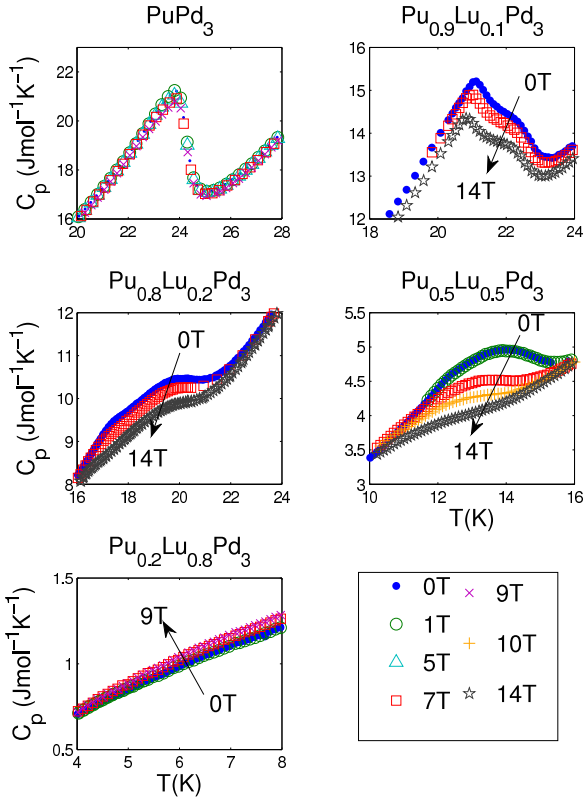

FIG. 6: (Color online) Heat capacity of $Pu_{1-x}Lu_xPd_3$ in applied magnetic field. The arrows indicate the direction of increasing field.

from a plot of C_p/T vs T^2 shown as an inset in figure 5. However, the magnetic heat capacity complicates the determination of γ because the Néel temperature is very low in some of the Lu-rich compounds. This increases the low temperature C_p and hence the estimate of γ from the straight line intercept. For this reason, for the Lu-rich compositions, we show the results of fitting the data in the region above T_N (γ^+) in addition to that below 8 K (γ^-) in table I. For Pu-rich compositions, the data above T_N will be affected by the Schottky anomaly at approximately 17 K, and will be unreliable. Thus it appears from these estimates that the electronic heat capacity decreases with increasing x after $x \approx 0.5$. The spread in the fitted parameters when data from different ranges of temperatures in the region $25 < T < 40$ K for γ^+, and $2 < T < 8$ K for γ^- was used was taken as an estimate of the errors in these parameters. This spread was found to be significantly larger than estimates of errors in the parameters from a covariance matrix derived from the measured error in C_p.

The Debye temperature θ_D from fitting the high temperature data, and appears to be independent of Lu-doping. This suggests that the phonon contribution to the heat capacity is constant through the series. A good estimate of this contribution is given by the heat capacity of the non-magnetic isostructural compound $LuPd_3$, which also has a negligible electronic heat capacity, $\gamma_{\rm Lu} = 3.5(5)$ mJmol^{-1}K^{-2}. We have thus extracted the additional electronic *and* magnetic heat capacity of $Pu_{1-x}Lu_xPd_3$ by sub-

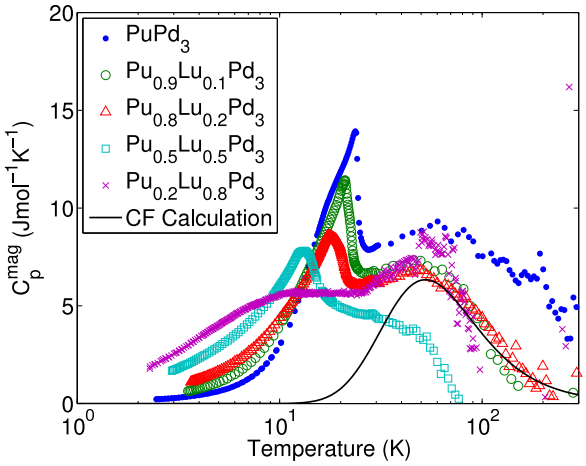

FIG. 7: (Color online) Deduced magnetic and electronic contribution to the heat capacity $C_p^{\rm mag} = C_p({\rm Pu}_{1-x}{\rm Lu}_x{\rm Pd}_3)$ - $(C_p({\rm LuPd}_3)$-$\gamma_{\rm Lu}^{+}T)$. The solid line is a crystal field calculation.

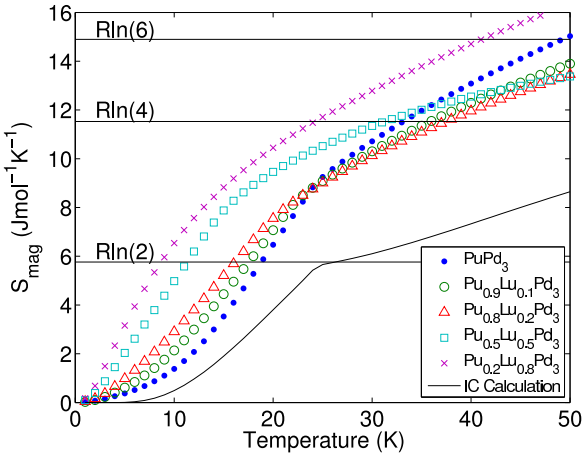

FIG. 8: (Color online) Deduced magnetic contribution to the entropy of $Pu_{1-x}Lu_xPd_3$, calculated by numerically integrating $C_p^{\rm mag}/T$.

tracting that of $LuPd_3$, as

$$C_p^{\rm mag} = C_p({\rm Pu}_{1-x}{\rm Lu}_x{\rm Pd}_3) - (C_p({\rm LuPd}_3) - \gamma_{\rm Lu}^{+}T) \quad (3)$$

This extracted quantity, scaled by the Pu concentration, is shown in figure 7.

The magnetic heat capacity for all the compounds shows a peak at ∼60 K, which we attribute to a Schottky anomaly from the crystal field (CF) splitting. The cubic CF on the Pu^{3+} ions splits the six-fold ground multiplet ($J = \frac{5}{2}$ in *LS*-coupling) into a doublet and quartet. The energy gap, $\Delta^{\rm CF}$, between these two levels determines the temperature of the Schottky peak, such that $\Delta^{\rm CF}$ ∼12 meV corresponds to a peak at 60 K. The magnitude of this peak, however, is determined by whether the doublet (C_p=6.3 $\rm Jmol^{-1}K^{-1}$) or quartet (C_p=2 $\rm Jmol^{-1}K^{-1}$) is the ground state. The data in figure 7 thus suggest a doublet ground state.

This is supported by the magnetic entropy, shown in figure 8, deduced by numerically integrating the magnetic heat capacity, $S(T) = \int_2^T \frac{C_p^{\rm mag}}{T} dT$. From the very low heat capacity of $PuPd_3$ at low temperatures, we believe the magnetic entropy from 0 to 2 K is negligble, and have not included this range in the integration. The value of the entropy at the Néel temperature is approximately $R\ln(3)$ for $PuPd_3$, which is above the value, $R\ln(2)$, expected for a doublet ground state. If the electronic heat capacity $\gamma_{\rm Pu}^{-} = 76$ $\rm mJmol^{-1}K^{-2}$ is subtracted from the integral, then we obtain $S(T_N) \approx R\ln(2.4)$. The remaining discrepancy may be due to (i) an incomplete subtraction of the phonon contribution, as the heat capacity of $LuPd_3$ may not be exactly analogous to the phonon heat capacity of $PuPd_3$, and (ii) a larger value of γ (see the discussion in section IV).

Finally, the inset to figure 5 shows what appears to be a hump at ∼17 K in the heat capacity of $PuPd_3$. This feature was initially attributed to the Schottky anomaly from the CF splitting in reference[5]. However it is more likely due to a Schottky anomaly from the splitting of the doublet ground state in the ordered phase, and indeed such a feature is observed in the mean field calculations in the next section. A splitting of $\Delta^{\rm MF} = 3.5$ meV gives a peak at ∼17 K, which is reasonable.

IV. MEAN FIELD CALCULATIONS

As noted in section III A, the measured effective moment for both $PuPd_3$ and the doped compounds is approximately 1 μ_B/Pu, in contrast to the expected *LS*-coupling value of $g_J\sqrt{J(J+1)} = 0.85\ \mu_B$ from a Hund's rule $^6H_{5/2}$ ground state for a Pu^{3+} ion. *LS*-coupling is a good approximation when both the Coulomb ($\mathcal{H}_C$) and spin-orbit ($\mathcal{H}_{so}$) interactions are large but $\mathcal{H}_C \gg \mathcal{H}_{so}$. In contrast, when $\mathcal{H}_C \ll \mathcal{H}_{so}$, *jj*-coupling is a better approximation, whereupon we obtain $\mu_{eff} = 2.86\ \mu_B$. In between these limits, for the case of intermediate coupling, the effective moment is a function of $\mathcal{H}_C$ and $\mathcal{H}_{so}$, and the full Hamiltonian, including both these terms and the crystal field ($\mathcal{H}_{cf}$) and Zeeman interactions ($\mathcal{H}_Z$) must be calculated.

The strength of $\mathcal{H}_C$ and $\mathcal{H}_{so}$, parameterised by the Slater (F^k) and spin-orbit (ξ) integrals, is fixed by the atomic environment of the unfilled shell electrons. Thus in practice, intermediate coupling refers to the case where the value of F^k and ξ are determined either from ab-initio (Hartree-Fock) calculations, or from experimental measurements using optical spectroscopy. Using parameters determined experimentally by Carnall from the spectra of dilute Pu^{3+} in $LaCl_3$[8], the effective moment is 1.44 μ_B. It is conceivable that in a metallic system like $Pu_{1-x}Lu_xPd_3$ there may be small changes to F^k and ξ compared to the insulating salts on which the measurements of[8] were made[9]. Nevertheless, a 10 % change in F^k and ξ to make the system more *LS*-like only yields μ_{eff} =1.38 μ_B. In order to obtain $\mu_{eff} \sim 1\ \mu_B$, we must double the magnitude of F^k and ξ compared to their measured values, which is probably unphysical.

Given that the crystal field interaction is small, as judged by the ∼12 meV split between the doublet ground state and first excited quartet deduced from the heat capacity measurements, $\mathcal{H}_{cf}$ has little effect on μ_{eff}. Thus we believe that the lower than expected effective moment is most likely due to Kondo screening. Nonetheless, a mean field calculation which can model the antiferromagnetic order and the single ion

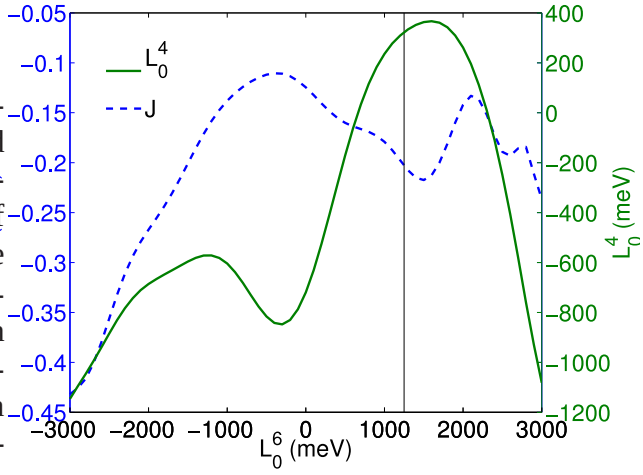

FIG. 9: (Color online) Calculated dependence of the CF parameter L_0^4 and the nearest neighbour exchange parameter $\mathcal{J}$ on L_0^6 subject to constraints described in the text. The vertical line indicates the optimal parameters.

intermediate coupling behaviour is still valuable to interpret the heat capacity and magnetisation data. Such a calculation, carried out using the *McPhase* package[10], is detailed below.

We have assumed a nearest neighbour only exchange interaction between $5f$ electrons, which is reasonable given the G-type antiferromagnetic structure where nearest neighbour moments align in antiparallel. Thus, there are three free parameters in the calculations: two crystal field (CF) parameters, L_0^4 and L_0^6, and one exchange parameter $\mathcal{J}$. There are two other non-zero CF parameters, but they are fixed by the cubic point symmetry of the Pu^{3+} ions such that $L_4^4 = \sqrt{5/14}L_0^4$ and $L_4^6 = -\sqrt{7/2}L_0^6$. It should be noted that the parameters used here correspond to the *Wybourne* normalisation[11], rather than the usual *Stevens* normalisation (usually denoted B_l^m). This is because the Stevens operator equivalents O_l^m are valid only within a single multiplet of given J, whereas we now require operators that can span all the allowed J values.

The two CF parameters are fixed by the requirement that they result in a doublet ground state with a quartet at ∼12 meV. This fixes a relation between L_0^4 and L_0^6 as shown in fig-

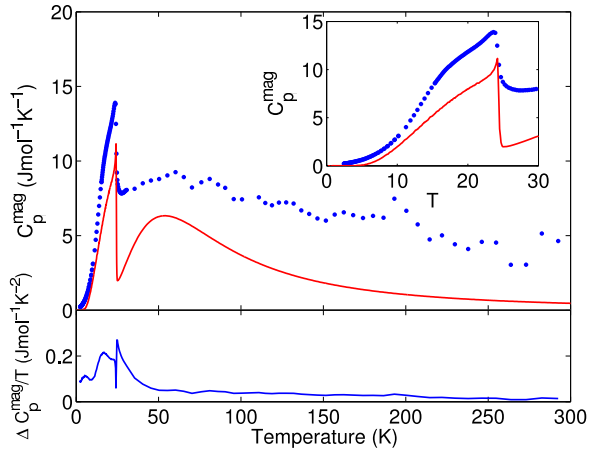

FIG. 10: (Color online) Measured and calculated magnetic heat capacity of $PuPd_3$. The estimated electronic heat capacity, $\Delta C_p^{\rm mag}/T = \frac{C_p^{\rm mag} - C_p^{\rm ic}}{T}$ is given in the bottom panel and has a mean value of 122 mJmol^{-1}K^{-2}.

ure 9. The Néel temperature T_N then fixes a relation between $\mathcal{J}$ and the crystal field parameters, and finally the magnetisation below T_N was used to fixed all three values, yielding $L_0^4 = 320$, $L_0^6 = 1250$, and $\mathcal{J} = -0.204$ meV.

The magnetisation is calculated by including in the Hamiltonian a Zeeman term, $-\mu_B\ (\mathbf{L} + 2\mathbf{S}) \cdot \mathbf{H}$; numerically diagonalising the energy matrix and calculating the expectation value of the moment operator $\mathbf{L} + 2\mathbf{S}$. The calculated inverse susceptibility is shown as a solid black line in figure 4 for comparison with the measured data. Unfortunately, better agreement with the data within the constraints of the mean-field intermediate coupling model is only possible by increasing the Coulomb or spin-orbit integrals to unphysical values. A more likely explanation is the suppression of the effective moment by Kondo screening, which is not considered in the current model.

The heat capacity is calculated by numerically differentiating the internal energy, $\langle U \rangle = \sum_n E_n \exp(-E_n/k_BT)/Z$, by the temperature, and the entropy by subsequently numerically integrating this. The calculated heat capacity, shown in figure 10, shows a shoulder around $\sim$20 K in accordance with the data which arises from a Schottky peak due to the splitting of the ground state doublet in the ordered phase. We can also estimate the electronic heat capacity by subtracting this calculated $C_p^{\rm ic}$ from the measured electronic and magnetic heat capacity, $C_p^{\rm mag}$, the result of which is shown in the bottom panel of figure 10. The spike near T_N is due to the differences in the sharpness of the calculated and measured transitions in this temperature range. Overall however, the mean value, $\overline{\gamma}$=122 mJmol^{-1}K^{-2}, over the full temperature range is in fair agreement with that derived from the low temperature heat capacity, $\gamma_{\rm Pu}$=76 mJmol^{-1}K^{-2}.

Similar mean-field heat capacity calculations for the other compositions, where the exchange coupling $\mathcal{J}$ was reduced to reflect the lower T_N, did not yield the broad transitions seen in figure 7, but rather the sharp lambda anomalies expected of an antiferromagnetic transition. Thus a subtraction to deduce their electronic specific heat becomes increasingly untenable. The broad transitions observed in the data are probably due to disorder in the system as a result of the Lu doping.

Finally, the calculated internal fields in the model are 226 T (180 T) at 1 K (20 K), which agree well with the molecular field of 217 T determined from fitting the measured resistivity using a simple CF model, as described in the next section.

V. ELECTRICAL TRANSPORT MEASUREMENTS

Electrical transport measurements were carried out using thin parallel-sided samples extracted after crushing the polycrystalline buttons produced by arc-melting. The first transport measurements were completed some months after the production of the samples, so there were significant aging effects in the Pu samples. This prompted us to re-anneal the $PuPd_3$ sample, and re-measure its resistivity, resulting in a large decrease in the residual resistivity ρ_0 from 225

$\mu\Omega$.cm to 11 $\mu\Omega$.cm. Subsequently the resistivity of the other compositions was also re-measured after re-annealing. The values of ρ_0 show a rapid increase with Lu doping up to $x = 0.5$ thereafter decreasing with x, as summarised in table II. This is due to the increasing number of defects caused by Lu substitution. Finally, measurements of the Hall coefficient and longitudinal resistivity of $PuPd_3$ and the x=0.1,0.2,0.5 compositions in field were also carried out.

The resistivity of $LuPd_3$ is well fitted by the Bloch-Grüneisen relation

$$\rho = C\frac{T^5}{\theta_D^6}\int_0^x \frac{x^5}{(e^x-1)(1-e^{-x})}dx \qquad (4)$$

where $x = T/\theta_D$, with $C = 181(1)$ $\mu\Omega$.cm and $\theta_D = 166(1)$ K. It was taken to be representative of the non-magnetic contribution to the resistivity of $Pu_{1-x}Lu_xPd_3$, and used to estimate the magnetic resistivity as $\Delta\rho = \rho(Pu_{1-x}Lu_xPd_3) - \rho(LuPd_3)$. This quantity is plotted in the case of zero applied magnetic field in figure 11. The in-field measurements showed little change from the zero field data, and the data for $PuPd_3$ agree well with previous measurements[12], albeit with a slightly lower residual resistivity.

Qualitatively, the behaviour of the resistivity may be divided into a high temperature Kondo-like regime, where the resistivity increases with decreasing temperature until ~50 K, followed by the onset of coherence, from where it falls sharply with temperature, and shows no clear anomaly at T_N. At low temperatures, the resistivity follows an exponential behaviour, in contrast to the T^2 dependence expected in a

Above ~70 K, the resistivity is well fitted by a $\rho_0 - \rho_1\log(T)$ term[13], where ρ_0 is the residual resistivity, and ρ_1 is proportional to the interaction between the conduction electrons and Kondo impurities. The fit is shown in figures 11 and 12, with parameters $\rho_0 = 235.8(3)\mu\Omega$.cm and $\rho_1 = 22(1)\mu\Omega$.cm for $PuPd_3$. The value of ρ_1 initially decreases with Lu doping to 15(2) $\mu\Omega$.cm for $x = 0.1$ and 16(2) $\mu\Omega$.cm for

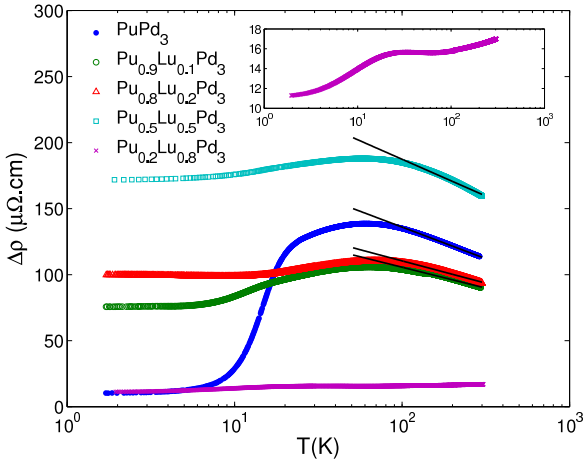

FIG. 11: (Color online) Zero-field magnetic resistivity of (Pu,Lu)Pd_3 on a logarithmic scale. Inset is an enlarged view of the $Pu_{0.2}Lu_{0.8}Pd_3$ composition.

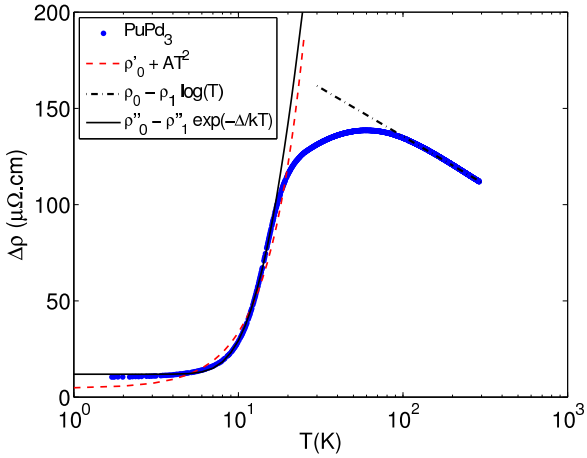

FIG. 12: (Color online) Zero-field magnetic resistivity of $PuPd_3$ on a logarithmic scale, with fits.

$x = 0.2$ but then increases to 27(3) $\mu\Omega$.cm for $x = 0.5$. This increase suggests that the Kondo interaction is strengthened at half doping.

The magnetic resistivity of $Pu_{0.2}Lu_{0.8}Pd_3$ does not show the Kondo behaviour of the other compositions, but rather increases with increasing temperature with a plateau region around 30-80 K. This behaviour and also the exponential temperature dependence of the low temper-

Composition	ρ_0 ($\mu\Omega$.cm)	$\rho_{s-f}^{(0)}$ ($\mu\Omega$.cm)	B_{mf} (T)	B_{mf}^{ic} (T)
$PuPd_3$	12.0(1)	876(37)	217(23)	226
$Pu_{0.9}Lu_{0.1}Pd_3$	75(1)	118(5)	88(4)	149
$Pu_{0.8}Lu_{0.2}Pd_3$	97(1)	35(1)	213(6)	143
$Pu_{0.5}Lu_{0.5}Pd_3$	172(1)	53(2)	92(5)	129
$Pu_{0.2}Lu_{0.8}Pd_3$	11.5(1)	17.8(1)	51(1)	88

TABLE II: Parameters for the spin-disorder resistivity model for $Pu_{1-x}Lu_xPd_3$ described in the text. The crystal field parameter B_4=0.041(1) meV was determined using the data for $PuPd_3$, and thereafter fixed in the fitting of the other compositions.

ature part of the resistivity, demonstrated in figure 12, is characteristic of a simple crystal field spin-disorder resistivity model[14]. This model is based on the scattering of conduction electrons with spin **s** by a localised moment **J** through an exchange interaction $-2G\mathbf{s}\cdot\mathbf{J}$, giving the resistivity in the first Born approximation as

$$\rho_{s-f} = \frac{3\pi N m^*}{\hbar e^2 E_F} G^2 (g-1)^2 \frac{1}{Z} \times \sum_{m_s,m_s',i,i'} \langle m_s', \psi_i' | \mathbf{s}\cdot\mathbf{J} | m_s, \psi_i \rangle p_i f_{ii'} \quad (5)$$

where the occupation factor for the crystal field level at E_i is $p_i = \exp(-\frac{E_i}{k_B T})$ and the conduction electron population factor is $f_{ii'} = 2[1+\exp(-\frac{E_i - E_{i'}}{k_B T})]^{-1}$. The wavefunctions $|\psi_i\rangle$ and energies E_i are determined by diagonalising the crystal field Hamiltonian.

In the absence of a crystal field, the $2J+1$ degenerate spin orbit ground state levels yield a temperature independent resistivity given by

$$\rho_{s-f}^{(0)} = \frac{3\pi N m^*}{\hbar e^2 E_F} G^2 (g-1)^2 J(J+1) \quad (6)$$

In our case, with a $J = \frac{5}{2}$ multiplet in a cubic crystal field, and in the absence of a magnetic field, equation (5) reduces to a sum of exponential functions, because the wavefunctions $|\psi_i\rangle$ are fixed, and the crystal field parameter can only change the splitting Δ^{CF} between the quartet and doublet. There is thus a universal behaviour, with the resistivity tending to $\rho_{s-f}^{(0)}$ at $T \gg \Delta^{CF}$, and then falling exponentially as the temperature falls below some level such that the excited crystal field states are no longer populated. This temperature is approximately $0.4\Delta^{CF}$, so the model suggests a splitting $\Delta^{CF} \approx 3.2$ meV, as the drop off in resistivity occurs around 15 K. This is significantly smaller than the splitting deduced from the Schottky peak at $\sim$60 K but is similar to the splitting of the ground state doublet (Δ^{MF}) in the ordered phase, as determined by the shoulder at $\sim$20 K in the heat capacity data.

In order to accommodate this splitting, we introduce a molecular field B_{mf} term. The low temperature exponential increase is then governed primarily by the split doublet, with a second exponential step at higher temperatures due to the crystal field splitting. It turns out that this second step is not observed in the case of $PuPd_3$ because the two steps merge into each other. Indeed a fit to the data below T_N with all parameters in the spin-disorder resistivity model varying freely yields a CF splitting of 14 meV, in agreement with the heat capacity data. As B_{mf} decreases in line with T_N with increasing Lu doping, whilst the CF splitting remains constant, the two steps become more pronounced in the calculations. These two steps are observed in the case of $Pu_{0.2}Lu_{0.8}Pd_3$, but the second step is masked by the Kondo screening in the other compositions.

Using this simple crystal field model we obtained the parameters shown in table II. Figure 13 shows the resulting fit to the data with ρ_0 subtracted. The CF splitting was fixed for all Lu doped compositions to the value determined from fitting the $PuPd_3$ data. The molecular field determined from mean field calculations, B_{mf}^{ic}, with exchange parameters $\mathcal{J}$ = -0.202, -0.199, -0.1925, and -0.174 meV, for compositions x=0.1,0.2,0.5 and 0.8 respectively, is also shown in the table. Apart from the case

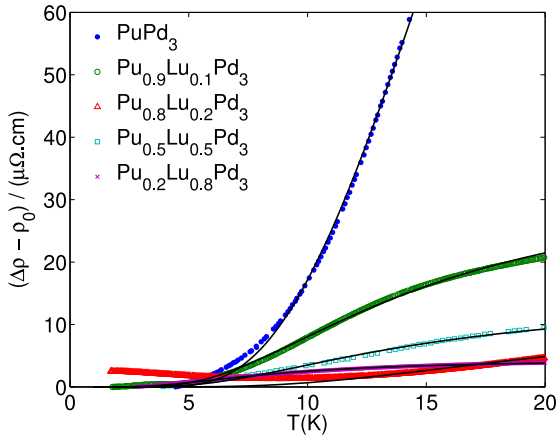

FIG. 13: (Color online) Zero-field magnetic resistivity of (Pu,Lu)Pd_3 with residual resistivity ρ_0 subtracted. Solid lines are fits using the crystal field model described in the text

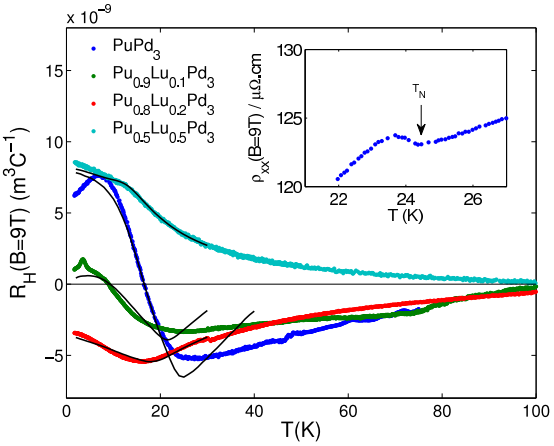

FIG. 14: (Color online) Temperature dependence of the Hall coefficient $R_H = \rho_{xy}/B$ and magnetoresistance at 9 T (inset). The solid black line is a fit using the measured magnetic susceptibility as described in the text

of $Pu_{0.8}Lu_{0.2}Pd_3$, the fitted $B_{\rm mf}$ is consistently lower than the calculated $B_{\rm mf}^{\rm ic}$. This is due to the overestimation of T_N in the mean field approximation, because we have estimated $\mathcal{J}$ from T_N, and $B_{\rm mf}^{\rm ic}$ is proportional to $\mathcal{J}$. Thus, $B_{\rm mf}^{\rm ic}$ is also overestimated.

$Pu_{0.8}Lu_{0.2}Pd_3$ shows an upturn at low temperatures, which cannot be accounted for by the current model. In addition, this upturn affects the fit by decreasing the ratio between the maximum and minimum resistivity, and hence $\rho_{\rm s-f}^{(0)}$. The exponential increase in the resistivity also occurs at a higher temperature and over a broader temperature range in this composition than in the others, which explains the anomalously high $B_{\rm mf}$. These features may be artefacts of the sample, because whilst an aged $Pu_{0.9}Lu_{0.1}Pd_3$ showed the upturn at low temperatures, the annealed sample did not, whereas both aged and annealed $Pu_{0.8}Lu_{0.2}Pd_3$ samples showed the upturn. Furthermore the resistivity of the aged $Pu_{0.8}Lu_{0.2}Pd_3$ sample is lower than that of the annealed sample. This suggests that the annealing had not fully repaired the radiation damage, and thus the resistivity may be strongly affected by crystallographic defects.

Nevertheless when the fits were repeated using the calculated $B_{\rm mf}^{\rm ic}$ as fixed parameters, the fitted $\rho_{\rm s-f}^{(0)}$ changed by less than 10%. The fits thus showed that the f-conduction electron interaction decreases with Lu doping, with a slight increase for the $x = 0.5$ composition compared to $x = 0.2$ and $x = 0.8$, in agreement with the fits to the Kondo parameter ρ_1.

$x =$	0	0.1	0.2	0.5
R_0	32.9(4)	12.1(2)	1.5(1)	0.9(1)
R_1	-6.97(8)	-2.31(3)	-0.74(1)	-0.028(1)

TABLE III: (Color online) Fitted Hall constants of $Pu_{1-x}Lu_xPd_3$. All values are in $(10^{-9}\mathrm{m}^3\mathrm{C}^{-1})$.

We now turn to the electrical transport properties in an applied magnetic field. The temperature dependence of the Hall coefficient R_H and the magnetoresistivity ρ_{xx} in 9T are shown in figure 14. $\rho_{xx}(T)$ follows the same behaviour as the zero field resistivity shown above, with the exception that there is a small peak just below the Néel temperature as shown in the inset to the figure. This was not observed previously and is reminiscent of the superzone scattering near T_N

in the heavy rare earths[15].

The temperature dependence of the Hall effect may be described phenomenologically by a scaling of the magnetisation, as in

$$\rho_{xy}(T) = R_0 B + R_1 \mu_0 M(T)$$

where R_0 is the *ordinary* and R_1 the *extraordinary* Hall constant. In figure 14, the solid lines show fits of the Hall coefficient to this relation using the measured magnetisation data. Both the ordinary and extraordinary Hall constants were found to decrease with Lu doping, as shown in table III. R_1 is proportional to the conduction-f electron exchange interaction strength G discussed above, so the decrease in its magnitude further indicates that this interaction becomes weaker with Lu doping.

VI. CONCLUSIONS

We have completed extensive bulk properties measurements on antiferromagnetic $PuPd_3$ and the pseudo-binary compounds $Pu_{1-x}Lu_xPd_3$. The transition temperature was found to decrease linearly from T_N =24.4(3) K in $PuPd_3$ to 7(2) K in $Pu_{0.2}Lu_{0.8}Pd_3$.

Heat capacity measurements show a Schottky anomaly at ∼60 K, which was interpreted as arising from a crystal field splitting between a doublet ground state and an excited state quartet at ∼12 meV. The deduced Sommerfeld coefficient, γ was found to be significantly higher than that expected for the free electron model, with a value of the order of 0.1 $Jmol^{-1}K^{-2}$ determined by fitting the data directly and by subtracting the calculated magnetic and measured phonon contributions. Direct fits to the data suggest that γ decreases with increasing Lu substitution. The magnetic heat capacity was calculated using a mean field model which showed that the shoulder in the data corresponds to a splitting of the doublet ground state in the ordered phase with a gap of ∼3.5 meV. The size of this gap is supported by fits of the resistivity to a crystal field model.

Magnetic susceptibility and magnetisation measurements also showed that the paramagnetic effective moment, $\mu_{\rm eff}$ increases with Lu concentration, approaching the value expected in intermediate coupling. These observations arise from the Kondo interaction which suppresses the effective magnetic moment but enhances the electronic effective mass, m^*. As the Kondo interaction decreases with Lu doping, $\mu_{\rm eff}$ is screened less, and $\gamma \propto m^*$ falls.

Electrical transport measurements support this decrease in the Kondo interaction with increasing Lu concentration, x, as parameters proportional to the f-conduction electron coupling in a crystal field model of the resistivity and Hall effect were found to fall as x increases.

Acknowledgements

We thank G.H. Lander and K. Gofryk for helpful discussions. M.D.L thanks the UK Engineering and Physical Sciences Research Council for a research studentship, and the Actinide User Lab at ITU. We are grateful for the financial support to users provided by the European Commission, DG-JRC within its "Actinide User Laboratory" program, and the European Community's Access to Research Infrastructures action of the Improving Human Potential Programme (IHP), Contracts No. HPRI-CT-2001-00118, and No. RITA-CT-2006-026176.

* Electronic address: duc.le@helmholtz-berlin.de

[1] H. C. Walker, K. A. McEwen, M. D. Le, L. Paolasini, and D. Fort, J. Phys.: Condens. Matter **20**, 395221 (2008).

[2] H. C. Walker, K. A. McEwen, P. Boulet, E. Colineau, J.-C. Griveau, J. Rebizant, and F. Wastin, Phys. Rev. B **76**, 174437 (2007).

[3] M. D. Le, H. C. Walker, K. A. McEwen, T. Gouder, F. Huber, and F. Wastin, J. Phys.: Con-

dens. Matter **20**, 275220 (2008).

[4] W. J. Nellis, A. R. Harvey, G. H. Lander, B. D. Dunlap, M. B. Brodsky, M. H. Mueller, J. F. Reddy, and G. R. Davidson, Phys. Rev. B **9**, 1041 (1974).

[5] M. D. Le, K. A. McEwen, F. Wastin, P. Boulet, E. Colineau, R. Jardin, and J. Rebizant, Physica B **403**, 1035 (2008).

[6] G. Raphael and R. Lallement, Sol. St. Comm. **6**, 383 (1968).

[7] B. McCart, G. H. Lander, and A. T. Aldred, J. Chem. Phys. **74**, 5263 (1981).

[8] W. T. Carnall, J. Chem. Phys. **96**, 8713 (1992).

[9] A. D. Taylor, R. Osborn, K. A. McEwen, W. G. Stirling, Z. A. Bowden, W. G. Williams, E. Balcar, and S. W. Lovesey, Phys. Rev. Lett. **61**, 1309 (1988).

[10] M. Rotter, J. Magn. Mag. Mat. **272-276**, 481 (2004).

[11] D. J. Newman and B. K. C. Ng, *Crystal Field Handbook* (Cambridge University Press, 2000).

[12] A. R. Harvey, M. B. Brodsky, and W. J. Nellis, Phys. Rev. B **7**, 4137 (1973).

[13] J. Kondo, Progress of Theoretical Physics **32**, 37 (1964).

[14] V. U. S. Rao and W. E. Wallace, Phys. Rev. B **2**, 4613 (1970).

[15] A. R. Mackintosh, Phys. Lett. **4**, 140 (1963).